Mon. Not. R. Astron. Soc. **000**, 000–000 (0000) Printed 5 February 2008 (MN LATEX style file v1.4)

A Survey of hard spectrum *ROSAT* sources 1: X–ray source catalogue

M.J. Page[1], J.P.D. Mittaz[1], F.J. Carrera[1,2]
[1] *Mullard Space Science Laboratory, University College London, Holmbury St Mary, Dorking, Surrey RH5 6NT, UK.*
[2] *Instituto de Física de Cantabria (Consejo Superior de Investigaciones Científicas–Universidad de Cantabria), 39005 Santander, Spain.*

ABSTRACT

We present a catalogue of 147 serendipitous X–ray sources selected to have hard spectra ($\alpha < 0.5$) from a survey of 188 *ROSAT* fields. Such sources must be the dominant contributors to the X-ray background at faint fluxes. We have used Monte Carlo simulations to verify that our technique is very efficient at selecting hard sources: the survey has ≥ 10 times as much effective area to hard sources as it has to soft sources above a 0.5 - 2 keV flux level of 10^{-14} erg cm^{-2} s^{-1}. The distribution of best fit spectral slopes of the hard sources suggests that a typical *ROSAT* hard source in our survey has a spectral slope $\alpha \sim 0$. The hard sources have a steep number flux relation ($dN/dS \propto S^{-\gamma}$ with a best fit value of $\gamma = 2.72 \pm 0.12$) and make up about 15% of all 0.5 - 2 keV sources with $S > 10^{-14}$ erg cm^{-2} s^{-1}. If their $N(S)$ continues to fainter fluxes, the hard sources will comprise $\sim 40\%$ of sources with 5×10^{-15} erg cm^{-2} s^{-1} $< S < 10^{-14}$ erg cm^{-2} s^{-1}. The population of hard sources can therefore account for the harder average spectra of *ROSAT* sources with $S < 10^{-14}$ erg cm^{-2} s^{-1}. They probably make a strong contribution to the X-ray background at faint fluxes and could be the solution to the X-ray background spectral paradox.

1 INTRODUCTION

Determining the origin of the extragalactic X–ray background (XRB) has been a major goal of X–ray astronomers for more than three decades since its discovery (Giacconi et al. 1962), and surveys of the soft X–ray sky with *Rosat* have succeeded in resolving $\sim 80\%$ of the 1-2 keV XRB into individual sources (Hasinger et al. 1998). For the brighter sources which produce $\sim 40\%$ of the XRB, X–ray spectroscopy and optical identification has been possible. The majority of these sources are active galactic nuclei (AGN) with broad emission lines, i.e. Seyfert 1 galaxies and QSOs. At the faintest fluxes probed, a population of narrow emission line galaxies (NELGs) has been detected (McHardy et al. 1998). It has been argued that many of these are also AGN, but with low luminosity or obscured broad line regions (Schmidt et al. 1998).

However, it is not possible to synthesise the entire XRB by extrapolating the observed source populations to faint fluxes, because the majority of the known sources have X–ray spectra which are softer than the background. This discrepancy is present for all energy bands between 0.5 and 40 keV, and the 0.5 - 2 keV band where the deepest surveys have taken place is no exception. The spectrum of the extragalactic background, as measured with past and current instruments between 1 and 10 keV, can be described by a power law $F_\nu \propto \nu^{-\alpha}$ where $\alpha = 0.4 \pm 0.1$ (Chen, Fabian & Gendreau 1997, Miyaji et al 1998). The integrated spectrum of the broad line AGN detected in current 0.5 - 2 keV X–ray surveys is much softer, a power law with $\alpha \geq 1$ (Mittaz et al. 1999, Ciliegi et al. 1994), while that of the faint 0.5 - 2 keV sources identified as NELGs is similar to the background: Romero-Colmenero et al. (1996) found $\alpha = 0.4 \pm 0.1$ and Almaini et al. (1996) $\alpha = 0.5 \pm 0.1$ for two independent X–ray selected NELG samples. The integrated spectrum of these two populations is softer than the spectrum of the X-ray background, hence much of the remaining background must be produced by sources with spectra which are harder than the mean spectra of currently identified NELGs and AGN. The composition of the hard source population has not yet been determined, although we might expect a significant overlap with the NELG population, because the fitted X–ray spectral slopes of individual NELGs show considerable scatter, and because faint optical galaxies make a significant fraction ($\sim 30 - 40\%$) of the remaining unresolved X–ray background in deep PSPC images (Roche et al. 1995, Almaini et al. 1997, Newsam et al. 1999).

Current models for the synthesis of the X–ray background propose that a large proportion of the remaining background sources are obscured AGN. Such sources would be expected to have both lower fluxes and harder spectra than the current source populations. From X-ray spectroscopy of a large sample of sources from the *ROSAT* International X–ray Optical Survey (RIXOS, Mason et al. 2000), Mittaz et al. (1999) concluded that at faint *ROSAT* fluxes ($< 10^{-14}$ erg cm^{-2} s^{-1}) $\sim 13\%$ of sources have

spectra harder than that of the background, compared with only $\sim 7\%$ at brighter fluxes. This is probably the bright tail of the hard source population that must make a substantial contribution to the background at even fainter fluxes. These *ROSAT* detected hard sources should therefore provide us with a preview of the XRB producing population. As relatively bright examples, they are likely to be much easier to study at all wavelengths than their more numerous, but fainter, cousins.

This paper describes the survey of *ROSAT* PSPC pointed observations for examples of this faint, hard spectrum population and presents the catalogue of hard spectrum sources. Optical identification, spectroscopy and imaging of these sources are the subjects of companion papers. We describe the construction of the source catalogue and the *ROSAT* data reduction method in Section 2. The Monte Carlo simulations which were used to calculate the effective area of the survey and quantify the spectral selection effects are described in Section 4. The results of the simulations are taken into account in Section 5 to derive the characteristic X–ray spectral properties of the hard sources, their source counts, and their contribution to the 1 - 2 keV XRB. The source catalogue is also presented in this section. The implications of our findings are discussed in Section 6, and our conclusions are presented in Section 7.

2 CONSTRUCTION OF THE X–RAY SOURCE CATALOGUE

2.1 General description

The primary goal of the survey is to investigate the properties of extragalactic sources which have X–ray spectra harder than the extragalactic background emission, because such sources must exist in abundance at faint fluxes to resolve the spectral paradox. We chose to construct our source catalogue using archival *ROSAT* PSPC data. This was well suited to our purposes: the *ROSAT* PSPC has sufficient energy resolution to effectively discriminate hard from soft sources, while the excellent spatial resolution means we can expect to make unambiguous optical identifications for many of the hard sources.

2.2 Choice of *ROSAT* observations

The *ROSAT* PSPC fields were chosen according to the following preferences: high Galactic latitude, low Galactic N_H, long exposure time, observation targets which did not fill a large fraction of the field of view, and sky positions suitable for optical follow up. Only PSPC observations with the 'open' filter were used, and observations targeted on the Magellanic clouds were excluded. Some 188 PSPC datasets were searched for hard sources; a complete list of these observations is given in table 1.

For maximum reliability and reproducibility only REV2 processed data have been used. For consistency every PSPC dataset was reduced using the same sequence of operations which will now be described.

Table 1. *ROSAT* observations searched for hard sources.

rp200921n00	rp900140n00	rp600541n00	rp800344n00
rp800482n00	rp800483n00	rp600025a01	rp701217a01
rp800367a01	rp800383n00	rp700423n00	rp300133n00
rp800486n00	rp900190n00	rp800304n00	rp600439n00
rp300334n00	rp800326n00	rp400080n00	rp600504n00
rp600107n00	rp701180a01	rp700920n00	rp201488n00
rp700468n00	rp700424a01	rp300004n00	rp700884n00
rp900138n00	rp201339n00	rp700448n00	rp701187n00
rp900495n00	rp700873n00	rp600133n00	rp701223n00
rp700185n00	rp600159a00	rp700924a01	rp600005n00
rp700049n00	rp700882n00	rp900352n00	rp700516a00
rp201094n00	rp300007a02	rp701036n00	rp700467n00
rp900632n00	rp300079n00	rp800368n00	rp800226n00
rp701356n00	rp800386n00	rp700275n00	rp900496a01
rp800316n00	rp600436n00	rp600163n00	rp200208n00
rp800388n00	rp150082n00	rp600006n00	rp201374a01
rp300016n00	rp300389n00	rp700101n00	rp200654n00
rp600106n00	rp900147n00	rp900339n00	rp201552n00
rp701407n00	rp701499n00	rp800469n00	rp900009a01
rp201367m01	rp600050n00	rp600108n00	rp600262a02
rp700277n00	rp700875n00	rp900137n00	rp201382n00
rp600270n00	rp900211n00	rp600546n00	rp700061n00
rp200329n00	rp700122n00	rp701000a01	rp701457n00
rp000049n00	rp000054n00	rp170154n00	rp700228n00
rp700232n00	rp200322n00	rp700223n00	rp700221n00
rp300137n00	rp200453n00	rp700264n00	rp700210n00
rp700255n00	rp700258n00	rp150046n00	rp700211n00
rp700248n00	rp400059n00	rp700208n00	rp701200n00
rp700546n00	rp701202n00	rp200721n00	rp100308n00
rp200076n00	rp700073n00	rp200091n00	rp400020n00
rp700263n00	rp700265a01	rp900213n00	rp900214n00
rp900215n00	rp700112n00	rp700120n00	rp700123n00
rp700230a01	rp700246n00	rp700547n00	rp700055n00
rp700099m01	rp300003n00	rp700329a01	rp700117n00
rp700436n00	rp700372n00	rp700319n00	rp700387n00
rp700391n00	rp700315n00	rp200510n00	rp700326n00
rp700358n00	rp700010n00	rp300158n00	rp201103n00
rp701048n00	rp700375n00	rp700216a00	rp700435a00
rp700376n00	rp700392n00	rp200774n00	rp700271n00
rp700510n00	rp700489n00	rp700384n00	rp700227n00
rp300135n00	rp700290n00	rp700473n00	rp701034n00
rp700531n00	rp201219n00	rp701092n00	rp700527n00
rp701055n00	rp400141n00	rp700774n00	rp700499n00
rp700506n00	rp700496n00	rp700389n00	rp200127a01
rp200468n00	rp200473n00	rp200474n00	rp300222n00
rp300287n00	rp300291n00	rp700262a00	rp700461n00
rp700540n00	rp700872n00	rp700887n00	rp701214n00

2.3 X–ray data reduction

Each PSPC dataset was first passed through the FTOOLS PCPICOR task to correct for PSPC spatial/temporal gain variations. The dataset was then converted to STARLINK ASTERIX format and reduced using the STARLINK ASTERIX package. The data were screened to remove times of poor attitude solution, high particle background, and high overall background countrate.

An image for source searching was then produced. We chose to use the central 20 arcminute radius region where the point spread function and sensitivity are best, and used only PI channels 19 - 201 so that 'ghost imaging' in channels below 19 would not degrade the positional resolution (Hasinger et al. 1993a, Snowdon et al. 1994). A mean background level was determined from relatively source free parts of the image, and the STARLINK PSS

source searching routine was used to find sources more than 4σ above this background.

Next, we proceeded using a method similar to that described in Mittaz et al. (1999) to derive the spectral parameters of the sources. Images were constructed in 3 X–ray energy bands: PI channels 11-41, 52-90 and 91-201. Source counts were extracted around each PSS source position in each of these 3 images. For most sources a 54 arcsecond radius source circle was used, corresponding to $\sim$ 90% of the counts from a point source. For sources with one or more contaminating sources nearby, the source circles were reduced in size to be non-overlapping. The overall background estimate for each energy band was obtained by first masking out all the sources, and then flattening the image by dividing by an exposure map constructed with the same good time intervals as the screened data. The expected number of background counts in each source circle (in each energy band) was then obtained by dividing the counts in the background image by the unmasked background area, then multiplying by the area of the source circle and the value of the exposure map at the position of the source circle. Because the background count collecting area was much larger than any of the source circles, the statistical uncertainty on the predicted number of background counts in the source circle is small compared to the poisson shot noise on the number of source and background counts within the source circle.

2.4 Spectral fitting

To obtain a useful characterization of the X–ray spectrum of each source, a power law model ($F_E = kE^{-\alpha}$) was fit to the 3 colour data. This model has two very useful properties for our study: it has only two free parameters (slope α and normalization k) leaving one degree of freedom when fitting the 3 colour data, and its shape can easily be compared to that of the extragalactic XRB which is well described by a power law model (see Section 3).

The fitting was performed using the method developed by Mittaz et al. (1999), which is based on the Cash statistic (Cash 1979), a maximum likelihood estimator appropriate for the Poisson regime. In this method, the best fit values for the parameters α and k are obtained by minimising the quantity:

$$C' = -2\sum_{i=1}^{3} obs_i \; log(pred_i) - pred_i \qquad (1)$$

where subscript i denotes the X–ray energy band, obs_i is the observed (source + background) counts within the source circle and $pred_i$ is the model predicted, (source + background) counts within the source circle, given by:

$$pred_i = PSF_i \times model_i(\alpha, k, N_H) + b_i \qquad (2)$$

PSF_i is the fraction of the point spread function contained within the source circle for energy band i calculated using the equations of Hasinger et al. (1994). $model_i$ is the model predicted source counts in energy band i for a power law of slope α, normalisation k, absorbed by Galactic N_H, obtained using the FTOOLS 'nh' program to interpolate the data of Dickey & Lockman (1990).

For each source a grid of $\Delta C'$ was used to generate joint confidence intervals for the fit parameters α and k, exactly as $\Delta\chi^2$ is used to produce confidence intervals in standard χ^2 fitting. It was desirable to obtain from each two dimensional confidence region a one dimensional confidence interval in α for our spectral selection criterion, and a one dimensional confidence interval in broadband (0.5 - 2.0 keV) flux, the standard flux measure in *ROSAT* PSPC surveys. Because these confidence contours are non-symmetric in many cases, one dimensional marginalised errors for α were obtained by integrating the two dimensional probability distributions along the k dimension (Loredo 1990 and references therein). Similarly, after transforming the probability distribution from (α,k) space to (α,Flux) marginalised errors on the Flux were obtained by integrating over the α dimension.

We refer the reader to Section 5 of Mittaz et al. (1999) for derivation of equations 1 and 2 and detailed discussion of the advantages of this method for fitting faint *ROSAT* source spectra. Our application of this method as a sample selection tool is discussed in Section 4.1.

2.5 Radial profile fitting

For each source detected by PSS in the channel 19-201 image, we constructed a radial profile with 5 arcsecond radial bins. We then fitted a model *ROSAT* PSPC point spread function appropriate for the source offaxis angle (Hasinger et al. 1993a) to the radial profile using χ^2 out to 1 arcminute. This was not used for selecting hard sources, but the value of the best fit χ^2/ν is a useful indicator as to whether a source is point-like, and is given in column 7 of Table 3 for each hard source.

3 CRITERIA FOR INCLUSION IN THE CATALOGUE

A source with spectral slope α_{-l}^{+u} is included in the sample if

$$\alpha + u < 0.5 \qquad (3)$$

In other words, the spectral criterion by which a source merits inclusion in our hard source sample is to have the entire of its 68% best fit confidence interval in α harder than the slope of the extragalactic background, which we take to be $\alpha = 0.5$.

A spectrum which satisfies this criterion would be expected to have a probability of $\alpha < 0.5$ of at least 84%; in practive most of the sources included are harder than this at a much higher level of confidence. For each source we have calculated the probability that its spectrum is harder than $\alpha = 0.5$ by integrating the marginalised one dimensional probability distribution in α up to $\alpha = 0.5$. This probability is given for each source in column 16 of Table 3.

Finally, in order to produce an unbiased sample of hard sources we rejected any hard sources which are, or are related to, the target of the PSPC observation in which they were found. For example, a number of the observation targets were bright optical galaxies and hard sources found within these optical galaxies were rejected, because they are probably X-ray sources within the galaxies.

4 MONTE CARLO SIMULATIONS

4.1 Effective area of the survey

The hard source sample is not 'flux limited' in the usual style of X-ray surveys. Indeed, the use of our hard spectral selection criterion means that the probability of a source at a given flux and with a given spectrum being included in the sample depends on 1) Galactic N_H, 2) exposure time, 3) background intensity and spectrum, 4) local source density (which may affect the size of the source extraction circle), 5) offaxis angle and of course 6) the source spectrum. Because items 1 - 3 differ considerably between PSPC observations, while number 6 is different for every source, imposing meaningful flux limits is impossible.

Instead we have estimated the total effective area of the survey, as a function of flux and spectrum, using Monte Carlo simulations. First, we calculated the geometric area of each field excluding the area covered by the observation target (see Section 3). Then, for every field we simulated 3 colour spectra of 4000 sources, with predetermined values of flux and spectral slope. All the other inputs to the simulation were chosen to reflect the real survey as far as possible. Exposure time and Galactic N_H were fixed at the values for the real PSPC field. Source offaxis angle was generated randomly. Each source was simulated with the background found in the real PSPC field and using the real exposure map. The source extraction circle size was taken to be that of the real source most similar in offaxis angle to the simulated source. These simulated 3 colour spectra were then fit with a power law model exactly as for the real sources, and tested with the spectral selection criterion given in Eq. 3. The fraction of simulated sources which pass this selection criterion is equivalent to the probability of a source in that field, with the input flux and spectral slope, being included in the hard survey. The effective area of the field, to sources of that flux and spectral slope, is therefore the fraction of simulated sources which pass Eq. 3 multiplied by the geometric area of the field. The total effective area of our survey is the sum of the effective areas of all the fields. Note that simulations for every field were included in the effective area calculation, including fields that did not contribute any real hard sources to the survey.

The simulations were performed with a grid of input fluxes and spectral slopes to produce the effective area curves for different spectral slopes given in Fig. 1. The simulations show for flux $S > 10^{-14}$ erg cm^{-2} s^{-1} the survey effective area for hard sources ($\alpha = 0.0$, $\alpha = -0.5$, or $\alpha = -1.0$, solid lines in Fig. 1) is at least 10 times larger than the effective area for typical ($\alpha = 1.0$) sources (dashed line in Fig. 1).

4.2 Recovery of source spectra and fluxes

Our spectral selection criterion will inevitably lead to some systematic bias between the actual and fitted fluxes and spectra of the sources which are selected. The simulations used to determine the effective area also allow us to investigate the relationship between sources' intrinsic spectra and fluxes, and those obtained after the fitting and selection procedure. This is important for reconstructing the $N(S)$ relation and for inferring the spectra of the hard sources. In this section, and throughout the rest of the paper, we use F to refer to the output fitted source flux, and S to refer to a source's input (intrinsic) flux, so the ratio of fitted to intrinsic flux is F/S.

The distributions of fitted spectral slopes and F/S ratios of hard sources with input spectral slopes of $\alpha = -1$ (solid histogram) and $\alpha = 0$ (dashed histogram) are shown in Fig. 2. For $S > 2 \times 10^{-14}$ erg cm^{-2} s^{-1} the input fluxes of the sources are well recovered ($\pm 20\%$) and the peaks of the distributions of output spectra are close to the input slopes. At fainter fluxes, the output fluxes are skewed to higher values than the input fluxes, and the distributions of output spectral slopes are almost indistinguishable, with almost all sources having a fitted α of < 0.

Fig. 3 shows the distributions of F/S and fitted spectra for marginally hard sources ($\alpha = 0.5$, solid histograms) and ordinary sources ($\alpha = 1$, dashed histogram) scattered into the hard survey by poisson noise (see Section 5.1). The simulated faint $\alpha = 1$ sources which are scattered into the survey show a particularly strong skew towards larger F/S; this is unfortunate because it increases the expected contamination of the sample by 'normal' sources (Section 5.1). At bright fluxes the $\alpha = 0.5$ sources enter the survey with a softer distribution of slopes than either the hard sources ($\alpha \leq 0$) or the scattered $\alpha = 1$ sources. At faint fluxes ($S \sim 10^{-14}$ erg cm^{-2} s^{-1}) the $\alpha = 0.5$ sources and scattered $\alpha = 1$ sources have distributions of fitted slope which are similar to each other and to those of harder sources. All these effects will be taken into account in Section 5.2 when we characterise the spectra of the real hard sources.

5 RESULTS

The catalogue of 147 serendipitous *ROSAT* hard sources which comprise our hard source sample is presented in Table 3. Source names are based on the *ROSAT* positions derived from PSS and are given in column 1. Column 2 gives the name of the *ROSAT* observation in which the hard source was detected, and column 3 gives the PSPC exposure time after screening (Section 2.3). The offaxis angle of the source is given in column 4. The positional uncertainty of the X-ray source, as determined by PSS, is given in column 5, and the PSS significance of the source (number of sigmas above the background level) is given in column 6. As an indicator of whether or not the source is point-like, χ^2/ν (where $\nu = 11$) from fitting the source radial profile with the PSPC point spread function (Section 2.5) is given in column 7. The size of the source circle used to extract the 3 colour spectrum (Section 2.3) is given in column 8. The numbers of counts within this radius for each of the 3 bands (channels 11-41, 52-90 and 91-201) are given in columns 9, 10 and 11 respectively, and the the predicted numbers of background counts for the same bands are given in columns 12, 13 and 14. The fitted spectral slope for the source and 68% uncertainty (Section 2.4) are given in column 15. The probability that the source has a spectrum harder than $\alpha = 0.5$ (Section 3) is given in column 16, and the fitted 0.5 - 2.0 keV flux of the source, with 68% errors (Section 2.4) is given in column 17. Finally, column 18 contains a flag as to whether the source

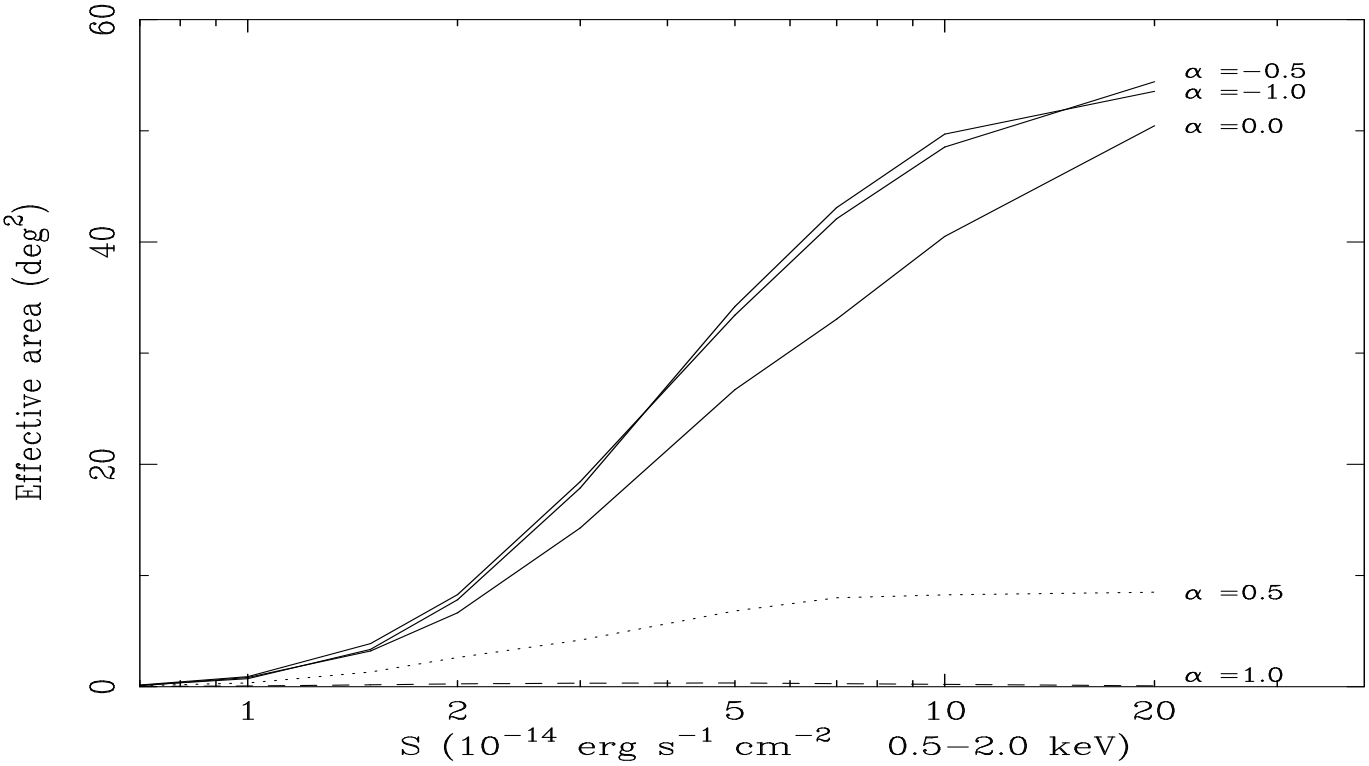

Figure 1. Effective area of the survey as a function of flux for sources with different power law spectral slopes α.

has a likely optical counterpart and will be used in subsequent papers about optical spectroscopy and imaging of the hard sources. 'S' means that the source is suitable for optical spectroscopy, while 'I' means that we consider the source only suitable for imaging follow up.

This sample represents the detection of a significant population of hard sources in *ROSAT*. Before we investigate their $N(S)$ relation, we will demonstrate that the contamination of the sample from non-hard sources is low, and determine an approximate characteristic spectral slope for the the hard source sample.

5.1 Contamination of the survey by non-hard sources

Although Fig. 1 shows that the survey is much more efficient at detecting hard sources than soft sources, the source population at the flux levels probed by *ROSAT* is dominated by sources which are softer than the background, with a mean spectrum of $\alpha \sim 1$ (eg Branduardi-Raymont et al. 1994, Hasinger et al. 1993b). Inevitably, poisson noise will scatter some soft sources into the hard survey; this is why the effective area of the survey to $\alpha = 1.0$ sources is non-zero. We constructed a 'worst case' estimate for the number of ordinary ($\alpha \sim 1$) sources scattered into the hard source survey by multiplying the $\alpha = 1$ effective area curve in Fig. 1 by the $N(S)$ relation of the entire X–ray source population (from Branduardi-Raymont et al 1994) and convolving with the $\alpha = 1$ distribution of F/S (see Section 4.2). The resultant predicted number of contaminant sources, as a function of flux, is compared to the actual source counts in Fig. 4. The predicted number of soft sources scattered into the survey reaches 19 (13% of the total) at the faint limit of our survey ($\sim 10^{-14}$ erg cm^{-2} s^{-1}).

In reality we expect the number of 'normal' soft sources scattered into our survey to be considerably smaller than this because:
1) The total $N(> S)$ includes hard sources which are not a contaminant.
2) The majority of the sources at $S > 10^{-14}$ erg cm^{-2} s^{-1} are AGN, and the more than half of these are actually softer than $\alpha = 1$ (eg see figure 7 of Mittaz et al. 1999) and so will be even more efficiently rejected by the spectral selection than the simulated $\alpha = 1$ sources.

We therefore expect that the level of contamination of the hard source sample by normal soft sources is small, $< 13\%$.

5.2 Characteristic X-ray spectral slope of the hard sources

The hard source survey has significant effective area to sources with almost any spectral slope $\alpha \leq 0.5$, but just *how hard* the source spectra are has a considerable bearing on their contribution to the XRB, and the possible origins of their X-ray spectra. Many of the sources are faint, with fairly large uncertainties on the fitted α, which will be biased by the spectral selection criterion (see Section 4.2). The sample probably contains objects with a range of spectra, but in this section we characterise our hard sample with a representative spectral slope. We determine this by looking for a value of intrinsic slope α which would give

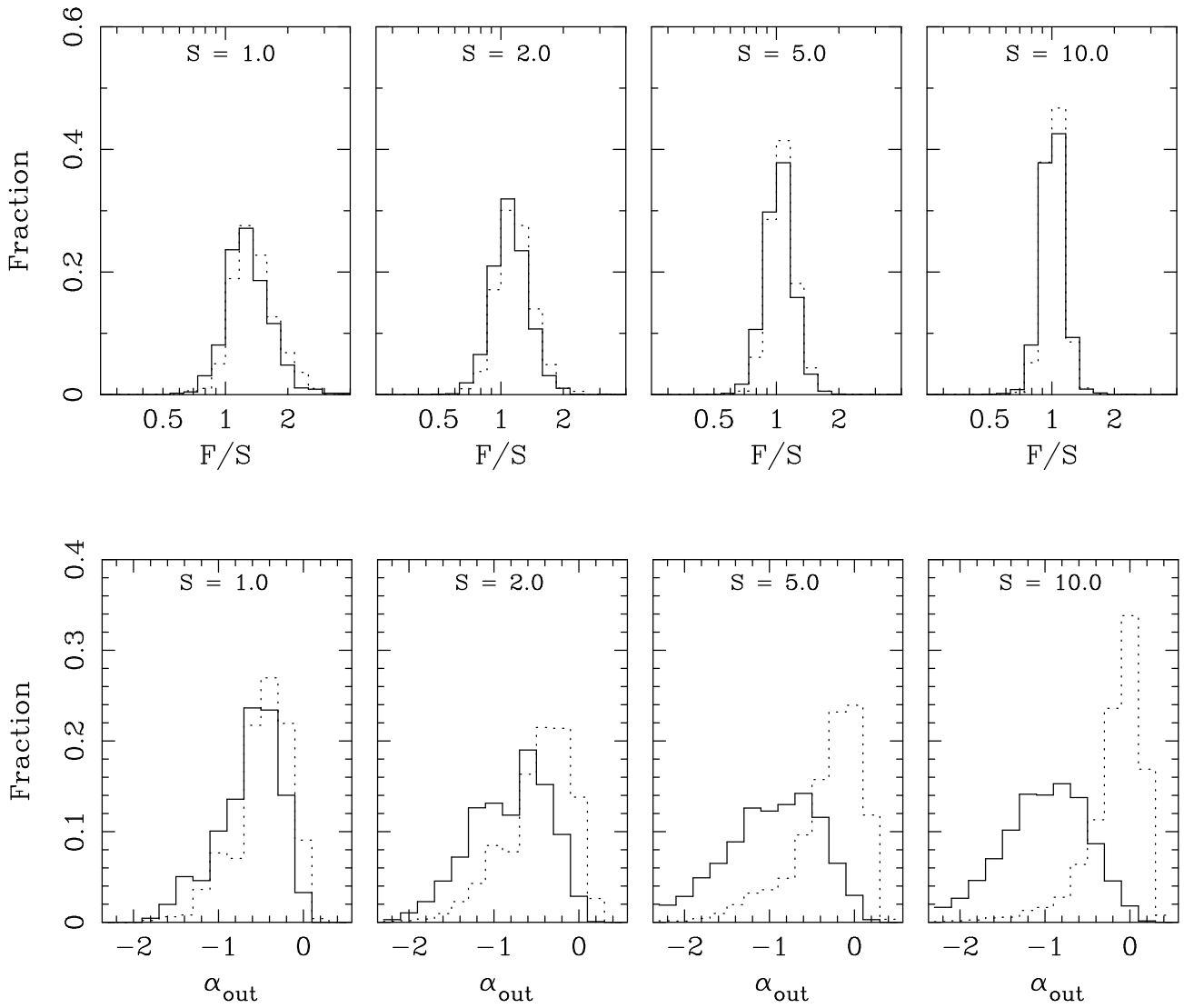

Figure 2. Distributions of F/S (top panel, where S is the intrinsic flux and F is the fitted flux) and fitted spectral slope (bottom panel) for simulated hard sources with intrinsic $\alpha = -1$ (solid histograms) and $\alpha = 0$ (dashed histograms) which achieve the spectral selection criterion (Eq. 3). Note that each histogram is normalised, and does not represent the sensitivity of the survey to those sources, which is given by Fig. 1.

rise to the observed distribution of fitted spectral slopes in the hard source sample.

Once again, we use our Monte Carlo simulations described in Section 4.2. For each value of the input spectral slope α, a distribution of fitted spectral slopes appropriate for the flux F of each hard source in the sample, was constructed from the simulations. This was done by linearly interpolating between the distributions of fitted slopes at discrete simulated fluxes. A simulated distribution of fitted spectra appropriate for the sample as a whole (for each value of intrinsic α) was then obtained by summing the simulated distributions for the individual hard sources.

To compare these simulated distributions of fitted spectral slopes with the real distribution, we used the Kolmogorov Smirnov (KS) test. The results of these comparisons are given in Table 2. The spectral slope which reproduces the distribution of fitted slopes best is $\alpha = 0$; all the other values for α are rejected by the KS test with $> 99.99\%$ confidence. Binned versions of the real distribution of spectral slopes and the intrinsic $\alpha = 0$ simulated distribution are shown in Fig. 5. Our hard source sample as a whole is therefore best characterised by a spectral slope of $\alpha \sim 0$; the sample is neither dominated by sources with similar spectra to that of the XRB ($\alpha \sim 0.5$) nor by sources which are *extremely* hard ($\alpha \leq -0.5$).

Table 2. KS test results comparing the distribution of fitted spectral slopes in the real sample, against distributions simulated assuming different intrinsic spectral slopes α

α	D_{max}	$P > D_{max}$
-1.0	0.40	6.9×10^{-21}
-0.5	0.22	7.2×10^{-7}
0.0	0.10	0.12
0.5	0.20	1.5×10^{-5}

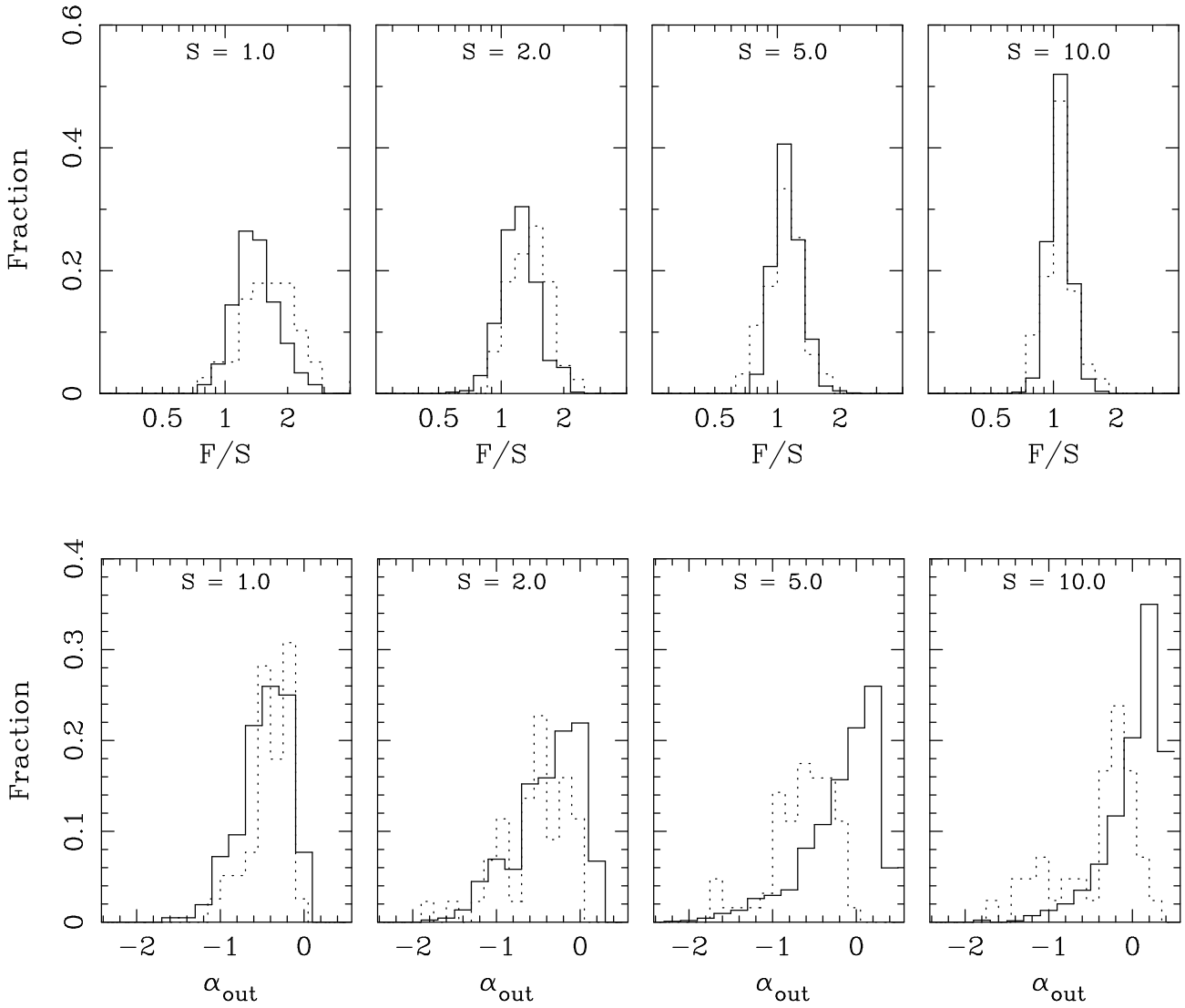

Figure 3. Distributions of F/S (top panel, where S is the intrinsic flux and F is the fitted flux) and fitted spectral slope (bottom panel) for simulated marginally hard sources ($\alpha = 0.5$, solid histograms) and soft sources ($\alpha = 1$, dashed histograms) which achieve the spectral selection criterion (Eq. 3). Note that each histogram is normalised, and does not represent the sensitivity of the survey to those sources, which is given by Fig. 1.

5.3 Source counts

The hard sources $N(S)$ (sky density of sources per unit flux, at flux S) is the critical issue as to whether the population of *ROSAT* hard sources are likely to contribute significantly to the XRB, and the solution to the spectral paradox, at faint fluxes. To derive the hard source $N(S)$, we use the $\alpha = 0$ effective area curve from Fig. 1, since we have already shown that $\alpha = 0$ best typifies the source spectra (Section 5.2). A power law model fit to the $N(S)$ relation was obtained using the Murdoch, Crawford and Jauncey (1973) maximum likelihood method for sources with measurement uncertainty. This is appropriate because we know from our simulations that the fitted fluxes (F) of the sources deviate from the actual fluxes (S) by more than 20% (see the top panel of Fig. 2). The method works by convolving the model $N(S)$ with the error distribution of the sample, to produce a model probability distribution of observed fluxes $P(F)$; the fitting proceeds by adjusting the shape of $N(S)$, hence $P(F)$, to maximise the likelihood of obtaining the sample's observed flux distribution.

The power law model $N(S)$ is defined as:

$N(S) = K\, S^{-\gamma}$

within the interval $S_{min} < S < S_{max}$. This is transformed to the model probability density $P(F)$ that a source in the sample will have observed flux F by:

$$P(F) = \frac{\int_{S_{min}}^{S_{max}} P(F \mid S)\ N(S)\ A(S)\ dS}{\int_{F_{min}}^{F_{max}} \int_{S_{min}}^{S_{max}} P(F \mid S)\ N(S)\ A(S)\ dS\ dF}$$

where $P(F \mid S)$ is the probability density of observed flux F given intrinsic flux S and $A(S)$ is the effective area to sources of intrinsic flux S. $P(F \mid S)$ and $A(S)$ were obtained from the Monte Carlo simulations. $F_{min} < F < F_{max}$ is the interval of observed flux in which the fitting was performed. To ensure that $P(F)$ is correctly determined close to F_{min} and F_{max}, S_{min} and S_{max} were set to

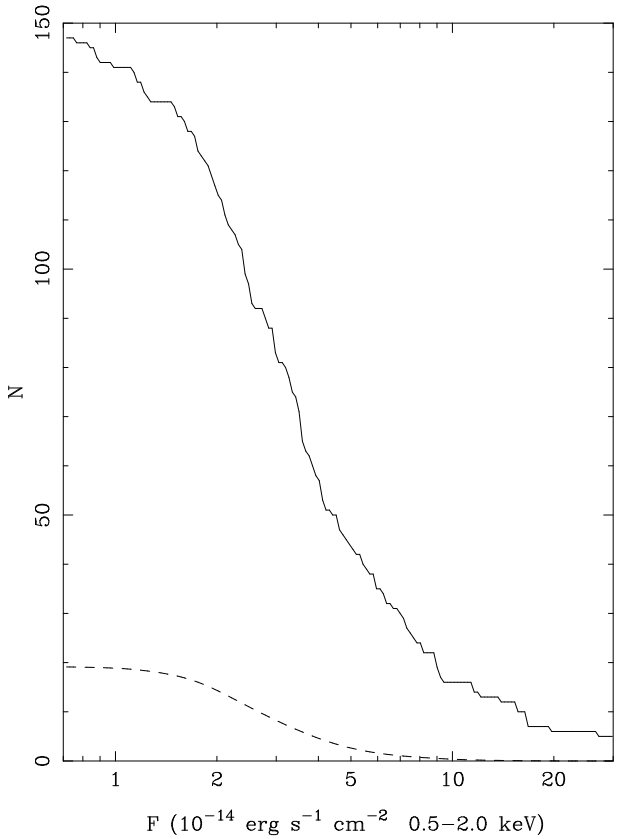

Figure 4. Worst case predicted number of contaminant $\alpha \sim 1$ sources (dashed line, see Section 5.1) compared to the actual content of the survey (solid line) as a function of observed flux F.

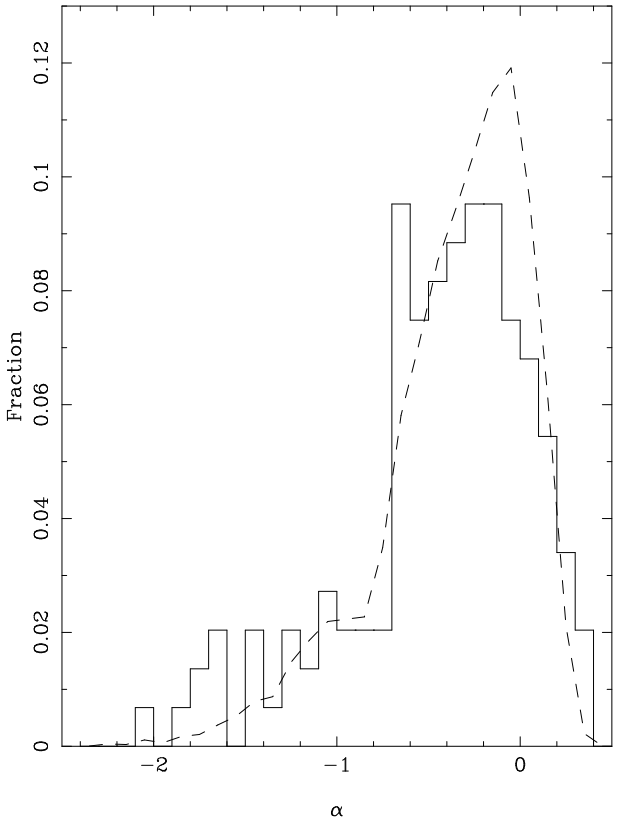

Figure 5. Distribution of hard source spectral slopes (solid histogram) and the simulated distribution for $\alpha = 0$ sources (dashed line).

50% and 200% of F_{min} and F_{max} respectively. We chose to fit the $N(S)$ with $F_{min} = 10^{-14}$ erg cm^{-2} s^{-1}, to minimise any contribution from sources fainter than the minimum flux of the effective area simulations, and $F_{max} = 2{\times}10^{-13}$ erg cm^{-2} s^{-1}, above which the sample may be incomplete due to our exclusion of *ROSAT* observation targets. The fit was performed by varying γ to maximise

$$P = \prod_{i=1}^{n} P(F_i)$$

where n is the number of sources with flux F_i with $F_{min} < F_i < F_{max}$. Estimates for the 68% and 95% uncertainty of γ were obtained by finding values for γ corresponding to $\Delta(-2\log(P)) = 1$ and 4 respectively. The normalisation K was determined by setting the number of observed sources to the number predicted:

$$K = \frac{n}{\int_{F_min}^{F_max} \int_{S_min}^{S_max} P(F \mid S)\ S^{-\gamma}\ A(S)\ dS\ dF}$$

The best fit value of γ is 2.72 ± 0.12 (±0.24 at 95%) with a normalisation $K = 32$ (10^{-14} erg cm^{-2} s^{-1})$^{(\gamma-1)}$deg^{-2}. The best fit model is shown in Fig. 6 along with the uncertainty bowtie corresponding to the 95% maximum likelihood fitting errors as well as a 95% normalisation error based on the number of sources in the sample. For reference, Fig. 6 also shows a crude $N(>S)$ for the hard sources obtained by

$$N(>S) \sim \sum_{i=1}^{n} 1/A(F_i) \quad (F_i > S)$$

(dots) as well as the best fit model $N(>S)$ for the overall source population (dashed line, from Branduardi-Raymont et al. 1994).

The best fit hard source $N(S)$ slope is steeper than the Euclidean value of $\gamma = 2.5$ and the model normalisation translates to $N(>10^{-14}$ erg cm^{-2} s$^{-1}) = 19$ deg^{-2}. The hard sources are therefore a significant component (> 10%) of the $S > 10^{-14}$ erg cm^{-2} s^{-1} 0.5 - 2 keV population.

5.4 Contribution to the 1-2 keV XRB

We have estimated the hard sources contribution to the 1-2 keV XRB, I_{1-2} from the fitted power law $N(S)$ from Section 5.3 assuming a spectral slope of $\alpha = 0$ (see Section 5.2).

$$I_{1-2} = \frac{2K(S_{min}^{(2-\gamma)} - S_{max}^{(2-\gamma)})}{3(2-\gamma)}$$

where K and γ are the normalisation and slope of the $N(S)$ as defined in Section 5.3 and S_{min} and S_{max} denote the 0.5 - 2 keV flux range of hard sources considered. We have assumed $S_{max} = 10^{-11}$ erg cm^{-2} s^{-1}.

For $S_{min} = 10^{-14}$ erg cm^{-2} s^{-1} (0.5 - 2 keV) the hard sources are responsible for a 1 - 2 keV intensity of $I_{1-2} = 1.0^{+0.3}_{-0.2} \times 10^{-9}$ erg s^{-1} cm^{-2} sr^{-1} (95% errors). Assuming the 1 - 2 keV XRB intensity is $\sim 1.45 \times 10^{-8}$

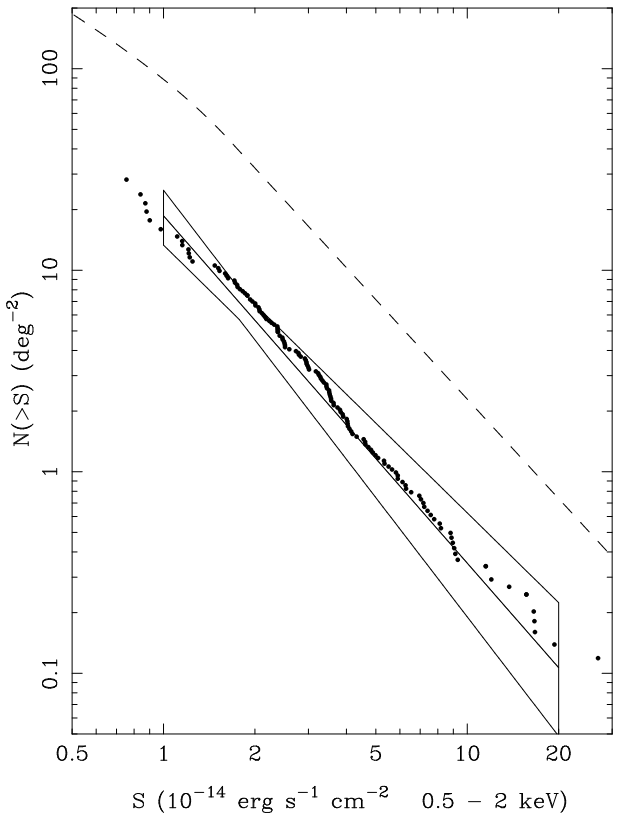

Figure 6. Best fit integral $N(>S)$ for the hard sources (solid line) along with 95% confidence interval (bowtie) and crude $N(>S)$ obtained by summing the inverse of the area available to each source (dots). Also shown for comparison is the $N(>S)$ of the whole population (dashed line, from Branduardi-Raymont et al. 1994)

erg s^{-1} cm^{-2} sr^{-1}, from the joint *ASCA ROSAT* spectral fits of Chen, Fabian & Gendreau (1997) and Mijayi et al. (1998), the hard sources contribute 7 ± 2% of the 1 - 2 keV background. Extrapolating the hard source $N(S)$ relation to $S = 10^{-15}$ erg cm^{-2} s^{-1} (0.5 - 2 keV), they would produce an intensity of $I_{1-2} = 5.1^{+5.1}_{-2.5} \times 10^{-9}$ erg s^{-1} cm^{-2} sr^{-1}, or 35^{+36}_{-16}% of the background. The hard sources therefore have the potential to be major contributors to the XRB at faint fluxes.

6 DISCUSSION

With the construction of our hard source catalogue, we have isolated a population of sources which have hard spectra ($\alpha \sim 0$), have a steep $N(S)$, and are numerous enough to make up $\sim$ 15% of sources with $S > 10^{-14}$ erg cm^{-2} s^{-1}. The total $N(S)$ of all sources in the 0.5 - 2 keV band has already flattened off to a sub-Euclidean slope by 10^{-14} erg cm^{-2} s^{-1} (Branduardi-Raymont et al. 1994, Hasinger et al. 1993). Extrapolating the hard source $N(S)$ shown in Fig. 6 to fainter fluxes, the hard source contribution increases to around 40% of all the sources between 0.5 and 1 $\times 10^{-14}$ erg cm^{-2} s^{-1}. This provides a very simple explanation for the hardening of the mean *ROSAT* source spectrum towards faint fluxes found by Mittaz et al. (1999), Vikhlinin et al. (1995) and Hasinger et al. (1993b).

The results presented here also offer a consistent picture of the source populations found in the *ROSAT* band and at higher energy. A long standing discrepancy has been the excess source counts in the 2-10 keV band compared to those in the 0.5-2 keV band (Warwick & Stewart 1989, Butcher et al. 1997). From the *ASCA* Large Sky Survey and *ASCA* Medium-Sensitivity Survey, Ueda et al. (1999a) and (1999b) recently showed that in the 0.7-7 keV energy range, sources with spectra harder than $\alpha = 0.7$ have a steeper $N(S)$ than softer spectrum sources. These harder sources make a small contribution to the source counts at very bright fluxes (< 20% at $> 10^{-12}$ erg cm^{-2} s^{-1}) but because of their steep $N(S)$ are almost as numerous as the soft sources at $S < 10^{-13}$ erg cm^{-2} s^{-1} (0.7-7 keV). Although the hard sources found in the 2-10 keV band have average energy spectra of $\alpha \sim 0.5 - 0.6$ (Ueda et al. 1999a, 1999b), softer than the *ROSAT* hard source spectra, they play a similar role in hardening the average source spectrum at faint fluxes.

The *ASCA* hard sources become significant at much brighter fluxes than the *ROSAT* hard sources. This is to be expected because hard spectrum sources contribute to higher energy source counts at brighter fluxes than soft sources; eg a source with $\alpha = 0$ is more than four times brighter in the 2-10 keV band than an $\alpha = 1$ source with the same 0.5 - 2 keV flux. Extrapolating the *ROSAT* hard source counts assuming $\alpha = 0$ results in ~ 5 sources deg^{-2} at 10^{-13} erg cm^{-2} s^{-1}(2 - 10 keV). The sky density of 2 - 10 keV sources at this flux level is between 10 and 20 deg^{-2} (Ueda et al. 1999a, 1999b, Georgantopoulos et al. 1998, Inoue et al. 1996). This means that the hard *ROSAT* population found by our survey could be a significant contributor to the 2 - 10 keV source counts, and that the *ROSAT* hard source population could constitute a large fraction of the *ASCA* hard sources as well. This hypothesis is supported by Ueda et al. (1999a and 1999b) finding that $\sim$ 80% of the *ASCA* sources detected in 2 - 10 keV are also detected in 0.7 - 2 keV, which implies that the population of hard *ASCA* sources *should* be found in the *ROSAT* band as well.

7 CONCLUSIONS

We have performed a survey of 188 *ROSAT* fields for sources with hard spectra ($\alpha < 0.5$), and present a serendipitous catalogue of 147 such hard sources. We have applied our spectral selection criterion to Monte Carlo simulations to calculate the effective area of our survey as a function of source flux and spectral slope. The Monte Carlo simulations have also been used to estimate biases in fitted flux and spectral slope resulting from the hard spectral selection. The effective area of the survey is at least 10 times greater for hard sources than for 'normal' $\alpha \sim 1$ sources for 0.5 - 2 keV source flux $S > 10^{-14}$ erg cm^{-2} s^{-1}. Convolving the overall $N(S)$ of 0.5 - 2 keV sources with the selection function of our survey, we show that the level of contamination of the sample by normal $\alpha \sim 1$ sources is small (≤ 15%). The distribution of hard sources fitted spectral slopes implies that a typical source in our

sample has a spectral slope $\alpha \sim 0$. The hard sources have a steep $N(S)$ relation ($dN/dS \propto S^{-\gamma}$ with a best fit value of $\gamma = 2.72 \pm 0.12$) and make up about 15% of all 0.5 - 2 keV sources with $S > 10^{-14}$ erg cm^{-2} s^{-1}. If their $N(S)$ continues to fainter fluxes, the hard sources will comprise $\sim$ 40% of sources with 5×10^{-15} erg cm^{-2} s^{-1}< S < 10^{-14} erg cm^{-2} s^{-1}. The increased contribution of hard sources to the faint *ROSAT* population can therefore account for the harder average spectra of *ROSAT* sources with $S < 10^{-14}$ erg cm^{-2} s^{-1}. The *ROSAT* hard source sample is probably the bright tail of the population that contributes much of the soft (and perhaps hard) X-ray background at faint fluxes. The *ROSAT* hard sources are probably a subset of the hard source population now detected in higher energy *ASCA* observations.

8 ACKNOWLEDGMENTS

FJC thanks the DGES for partial financial support, under project PB95-0122. This research has made use of data obtained from the Leicester Database and Archive Service at the Department of Physics and Astronomy, Leicester University, UK. This research has also made use of the NASA/IPAC Extragalactic Database (NED) which is operated by the Jet Propulsion Laboratory, California Institute of Technology, under contract with the National Aeronautics and Space Administration. We thank Dr Andrew Phillips for constructing the MSSL 'Beowulf' parallel computer which was invaluable for our Monte Carlo simulations.

9 REFERENCES

Almaini O., Shanks T., Boyle B.J., Griffiths R.E., Roche N., Stewart G.C., Georgantopoulos I., 1996, MNRAS, 282, 295

Almaini O., Shanks T., Griffiths R.E., Boyle B.J., Roche N., Georgantopoulos I., Stewart G.C., 1997, MNRAS, 291, 372

Branduardi-Raymont G., et al. , 1994, MNRAS, 270, 947

Butcher J.A., et al. 1997, MNRAS, 291, 437

Chen L.W., Fabian A.C., Gendreau K.C., 1997, MNRAS, 285, 449

Ciliegi P., Elvis M., Wilkes B.J., Boyle B.J., McMahon R.G., Maccacaro T., 1997, MNRAS, 284, 401

Georgantopoulos I., et al. 1997, MNRAS, 291, 203

Giacconi R. et al. , 1962, Phys. Rev. Letters, 9, 439.

Hasinger G., Boese G., Predehl P., Turner T.J., Yusaf R., George I.M., Rohrbach G., 1993a, MPE/OGIP Calibration Memo CAL/ROS/93-015

Hasinger G., Burg R., Giacconi R., Hartner G., Schmidt M., Trümper J., Zamorani G., 1993b, A&A, 275, 1

Hasinger G., Burg R., Giacconi R., Schmidt M., Trümper J., Zamorani G., 1998, A&A, 329, 482

Inoue H., Kii, T., Ogasaka Y., Takahashi T., Ueda Y., 1996, in Zimmerman U., Truṁper J.E., Yorke H., eds, Roïtgenstrahlung from the Universe, MPE Report 263, p. 323

Mason K.O. et al. , 2000, MNRAS, in press

Miyaji T., Ishisaki Y., Ogasaka Y., Ueda, Y., Freyberg M.J., Hasinger G., Tanaka Y., 1998, A&A, 334, L13

Mittaz J.P.D. et al. , 1999, MNRAS, 308, 233

Newsam, A.M., McHardy I.M., Jones L.R., Mason K.O., 1999, MNRAS, 310, 255

Roche N., Griffiths R.E., della Ceca R., Shanks T., Boyle B.J., Georgantopoulos I., Stewart G.C., 1996, MNRAS, 282, 820

Romero Colmenero E., Branduardi-Raymont G., Carrera F.J., Jones L.R., Mason K.O., McHardy I.M., Mittaz J.P.D., 1996, MNRAS, 282, 94

Schmidt M., Hasinger G., Gunn J., Schneider D., Burg R., Giacconi R., Lehmann I., MacKenty J., Trümper J., Zamorani G., 1998, A&A, 329, 495

Snowden S.L., McCammon D., Burrows D.N., Mendenhall J.A., 1994, ApJ, 424, 714

Vikhlinin A., Forman W., Jones C., Murray S., 1995, ApJ, 451, 564

Warwick R.S., Stewart G.C., 1989, ESA SP-296, 2, 727

Table 3. Hard source catalogue

1 Source	2 ROR	3 Exp (ks)	4 Offax (′)	5 Perr (″)	6 σ	7 PSF $\chi^2_{/\nu}$	8 r (″)	9 c1	10 c2	11 c3	12 b1	13 b2	14 b3	15 α	16 P < 0.5	17 Flux 0.5-2	18 Spl
RXJ000417.24-255915.1	rp700467n00	31.7	12.7	11.2	5.2	1.6	54	51	26	32	66.4	9.9	7.9	$-0.45^{+0.66}_{-0.56}$	0.99	$1.6^{+0.4}_{-0.3}$	I
RXJ000721.30+204326.5	rp700101n00	20.8	13.7	6.6	4.9	1.2	43	20	9	20	20.5	4.5	3.4	$-0.60^{+1.06}_{-1.60}$	0.92	$1.8^{+0.6}_{-0.5}$	I
RXJ001111.73-361840.1	rp800388n00	20.9	6.7	6.2	8.8	0.5	54	48	14	29	40.7	5.1	3.9	$-0.28^{+0.68}_{-0.75}$	0.99	$2.2^{+0.5}_{-0.4}$	I
RXJ001144.43-362638.0	rp800388n00	20.9	5.3	3.4	15.6	1.1	54	54	27	50	40.7	5.1	3.9	$-0.14^{+0.27}_{-0.35}$	1.00	$4.2^{+0.6}_{-0.6}$	S
RXJ004651.98-204329.0	rp600159a00	9.0	4.6	1.6	31.3	2.1	54	59	74	79	16.4	3.0	2.3	$0.33^{+0.13}_{-0.11}$	0.94	$19.4^{+2.0}_{-1.6}$	S
RXJ005726.44+270124.4	rp700884n00	18.9	15.8	7.3	9.4	0.9	54	19	15	45	16.7	6.7	8.2	$-0.91^{+1.10}_{-1.02}$	0.97	$4.6^{+1.1}_{-0.8}$	I
RXJ005732.46-273005.8	rp701223n00	43.7	8.3	6.9	6.0	1.7	25	18	6	19	16.2	2.4	1.7	$-0.90^{+1.22}_{-1.38}$	0.98	$0.8^{+0.2}_{-0.2}$	I
RXJ005734.78-272827.4	rp701223n00	43.7	10.0	3.9	9.1	1.4	50	59	19	32	57.5	8.5	5.9	$-0.34^{+0.56}_{-0.99}$	0.97	$1.2^{+0.3}_{-0.2}$	S
RXJ005736.38+302355.2	rp700424a01	17.0	3.8	5.7	8.0	1.7	40	5	7	19	9.4	2.8	2.0	$-0.89^{+0.92}_{-1.61}$	0.96	$1.9^{+0.6}_{-0.5}$	S
RXJ005736.81-273305.9	rp701223n00	43.7	5.6	6.8	7.1	0.5	50	62	26	33	60.6	8.9	6.2	$0.00^{+0.36}_{-0.64}$	0.94	$1.2^{+0.2}_{-0.2}$	S
RXJ005746.75-273000.8	rp701223n00	43.7	9.3	4.1	8.7	1.5	54	62	39	41	63.0	9.3	6.4	$0.08^{+0.34}_{-0.32}$	0.95	$1.7^{+0.3}_{-0.3}$	S
RXJ005801.64-275308.6	rp701223n00	43.7	16.4	5.2	14.7	1.0	54	67	47	99	57.4	8.4	5.9	$-0.36^{+0.31}_{-0.29}$	1.00	$5.1^{+0.5}_{-0.5}$	S
RXJ005808.69-273535.2	rp701223n00	43.7	9.3	5.0	6.1	1.1	36	23	13	21	26.5	3.9	2.7	$-0.36^{+0.71}_{-0.74}$	0.97	$0.9^{+0.2}_{-0.2}$	I
RXJ005812.20-274217.8	rp701223n00	43.7	10.4	7.7	5.9	1.0	54	58	20	26	63.2	9.3	6.5	$-0.30^{+0.58}_{-1.02}$	0.96	$0.9^{+0.2}_{-0.2}$	I
RXJ005830.02+263921.9	rp700884n00	18.9	12.9	2.3	21.5	1.6	54	21	25	116	18.0	7.3	8.8	$-1.69^{+0.70}_{-0.56}$	1.00	$11.5^{+1.6}_{-1.2}$	S
RXJ010742.15+322642.5	rp600106n00	23.4	4.4	3.0	11.6	3.6	18	5	11	38	4.9	2.4	3.4	$-0.64^{+0.82}_{-0.84}$	0.96	$3.5^{+0.8}_{-0.5}$	S
RXJ010908.73+192759.5	rp201488n00	12.9	14.8	12.2	5.3	1.7	50	9	8	17	13.1	3.1	2.7	$-0.56^{+0.98}_{-1.30}$	0.94	$2.5^{+0.9}_{-0.6}$	S
RXJ013555.47-183210.2	rp200208n00	24.8	15.1	8.5	8.8	0.9	54	55	21	41	49.0	8.1	4.5	$-0.53^{+0.45}_{-0.75}$	1.00	$3.2^{+0.6}_{-0.6}$	S
RXJ013707.63-183846.4	rp200208n00	24.8	17.6	10.0	10.2	1.1	54	55	26	44	45.3	7.5	4.1	$-0.23^{+0.30}_{-0.47}$	1.00	$4.0^{+0.7}_{-0.6}$	S
RXJ013717.52-182716.9	rp200208n00	24.8	9.6	4.0	8.6	1.0	18	8	4	19	5.9	1.0	0.5	$-0.98^{+1.12}_{-1.33}$	1.00	$2.5^{+0.7}_{-0.6}$	I
RXJ013721.47-182558.3	rp200208n00	24.8	9.8	2.6	15.4	1.6	36	37	31	46	22.6	3.8	2.1	$0.03^{+0.19}_{-0.27}$	0.99	$3.9^{+0.6}_{-0.5}$	S
RXJ014159.22-543037.0	rp800383n00	7.4	11.8	3.4	11.9	0.9	54	21	18	36	18.4	3.1	3.7	$-0.22^{+0.41}_{-0.57}$	0.98	$8.8^{+1.5}_{-1.5}$	S
RXJ021658.11-173203.3	rp900352n00	9.1	14.4	14.8	5.3	0.8	54	7	9	15	9.8	1.5	1.5	$-0.35^{+0.51}_{-0.94}$	0.96	$3.3^{+0.8}_{-0.9}$	I
RXJ023313.71+005536.0	rp800482n00	24.9	12.6	6.2	9.3	3.1	54	36	19	34	35.9	4.4	4.2	$-0.06^{+0.45}_{-0.65}$	0.93	$2.5^{+0.4}_{-0.4}$	S
RXJ023851.91-520958.8	rp701356n00	21.3	16.3	13.1	7.6	1.5	54	36	24	48	39.2	5.0	5.5	$-0.25^{+0.50}_{-0.50}$	0.98	$4.9^{+0.9}_{-0.6}$	S
RXJ025753.52+194442.2	rp900138n00	21.2	12.8	3.3	17.1	1.1	54	30	27	92	28.7	4.0	2.9	$-0.53^{+0.50}_{-0.57}$	0.98	$9.3^{+1.1}_{-0.9}$	I
RXJ025755.08+194255.5	rp900138n00	21.2	14.0	4.7	14.7	0.8	54	33	15	88	28.0	3.9	2.8	$-1.86^{+0.75}_{-0.79}$	1.00	$9.1^{+1.4}_{-1.0}$	I
RXJ031043.21-472033.4	rp800304n00	7.7	8.7	14.5	4.3	1.4	54	17	6	12	18.3	2.2	2.3	$-0.54^{+0.89}_{-1.50}$	0.95	$2.4^{+0.9}_{-0.8}$	S
RXJ031114.91-473150.0	rp800304n00	7.7	3.9	9.8	5.6	0.7	47	13	5	10	13.2	1.6	1.7	$-0.41^{+0.89}_{-1.48}$	0.93	$2.0^{+0.9}_{-0.7}$	I
RXJ031456.58-552006.8	rp701036n00	40.6	6.6	3.6	12.6	0.9	54	101	23	82	93.3	9.6	6.1	$-1.66^{+0.70}_{-0.85}$	1.00	$3.5^{+0.5}_{-0.5}$	S
RXJ031956.76-663938.5	rp600504n00	14.1	14.0	60.0	15.4	1.6	54	16	23	64	12.9	3.5	3.9	$-0.44^{+0.50}_{-0.48}$	1.00	$8.9^{+1.3}_{-1.0}$	I
RXJ033340.22-391833.4	rp800367a01	14.8	14.5	7.6	8.5	1.4	54	37	12	29	30.0	3.7	3.7	$-0.24^{+0.71}_{-0.77}$	0.98	$3.4^{+0.7}_{-0.7}$	S
RXJ033350.25-390850.9	rp800367a01	14.8	10.5	7.6	7.4	1.2	32	14	12	18	11.5	1.4	1.4	$0.02^{+0.40}_{-0.56}$	0.93	$2.8^{+0.7}_{-0.6}$	S
RXJ033402.54-390048.7	rp800367a01	14.8	13.9	4.9	12.8	2.3	50	34	33	50	25.5	3.1	3.2	$-0.06^{+0.30}_{-0.23}$	1.00	$7.2^{+1.0}_{-0.9}$	S
RXJ033729.08-253056.2	rp300079n00	41.7	11.6	10.1	4.7	1.5	50	100	30	25	96.9	15.7	5.3	$0.03^{+0.45}_{-0.82}$	0.93	$1.0^{+0.2}_{-0.2}$	I
RXJ033736.63-252052.2	rp300079n00	41.7	4.2	5.0	8.8	1.1	40	61	26	36	62.8	10.2	3.4	$-0.51^{+0.55}_{-0.56}$	1.00	$1.5^{+0.3}_{-0.2}$	S
RXJ033827.42-252400.0	rp300079n00	41.7	7.9	1.6	26.2	0.9	54	110	80	143	105.3	17.1	5.8	$-0.62^{+0.18}_{-0.27}$	1.00	$6.3^{+0.5}_{-0.5}$	S
RXJ034043.77-183457.5	rp600163n00	17.7	7.5	3.7	14.4	1.0	54	30	22	56	27.6	9.9	10.7	$-0.68^{+0.70}_{-1.01}$	0.97	$4.8^{+1.1}_{-0.6}$	I
RXJ034110.98-445654.0	rp900495n00	45.0	10.6	8.0	6.0	2.0	29	27	8	25	27.8	2.6	1.9	$-1.00^{+0.86}_{-1.20}$	0.99	$1.2^{+0.3}_{-0.3}$	I
RXJ034119.02-441033.3	rp900632n00	42.3	9.9	4.1	11.4	1.7	22	20	21	33	16.1	1.8	1.0	$0.06^{+0.34}_{-0.34}$	0.96	$2.6^{+0.4}_{-0.4}$	S
RXJ034130.14-450309.8	rp900495n00	45.0	11.1	6.2	7.6	1.3	43	51	18	30	59.6	5.7	4.1	$-0.47^{+0.71}_{-0.60}$	0.99	$1.2^{+0.2}_{-0.3}$	I
RXJ034248.22-450507.2	rp900495n00	45.0	12.5	14.3	4.7	2.0	54	84	15	26	86.8	8.3	6.0	$-0.59^{+0.85}_{-1.40}$	0.97	$0.9^{+0.2}_{-0.2}$	I
RXJ043420.48-082136.7	rp700290n00	6.5	14.1	7.0	10.7	2.3	54	24	10	38	22.3	3.4	1.8	$-1.17^{+1.21}_{-0.95}$	0.98	$11.5^{+2.7}_{-1.8}$	S
RXJ045304.40-531710.5	rp600436n00	21.8	11.3	8.5	5.6	0.6	50	37	7	21	32.0	3.1	2.8	$-0.80^{+1.07}_{-1.79}$	0.91	$1.6^{+0.5}_{-0.4}$	S
RXJ045558.99-753229.1	rp200921n00	22.8	18.0	1.9	63.7	8.0	54	25	87	719	19.6	6.3	4.7	$-2.43^{+0.26}_{-0.26}$	1.00	$90.8^{+4.9}_{-3.9}$	S
RXJ052839.93-325148.5	rp300004n00	6.8	10.1	5.5	7.9	1.8	36	8	18	20	6.1	2.1	0.6	$0.09^{+0.40}_{-0.38}$	0.92	$7.2^{+1.4}_{-1.4}$	S
RXJ053018.72-462509.7	rp300334n00	32.1	13.4	7.2	10.5	1.8	54	43	18	46	44.4	7.4	6.7	$-0.73^{+0.66}_{-1.10}$	0.98	$2.5^{+0.5}_{-0.4}$	S
RXJ053219.84-462550.5	rp300334n00	32.1	7.8	4.9	10.2	1.1	54	51	14	40	45.1	7.5	6.8	$-1.08^{+1.24}_{-1.26}$	0.97	$2.0^{+0.5}_{-0.4}$	I
RXJ053242.79-462400.9	rp300334n00	32.1	11.5	7.7	6.5	1.1	54	51	12	35	42.1	7.0	6.3	$-1.17^{+1.11}_{-1.82}$	0.95	$1.8^{+0.5}_{-0.4}$	I
RXJ082640.20+263112.3	rp200453n00	13.7	7.2	5.2	10.2	1.0	54	14	8	30	17.3	2.3	2.1	$-1.27^{+0.93}_{-1.06}$	1.00	$3.8^{+0.8}_{-0.9}$	S
RXJ085240.51+134651.8	rp700887n00	17.7	9.2	1.7	19.1	2.4	54	22	45	71	26.1	3.5	3.6	$-0.02^{+0.25}_{-0.32}$	0.98	$8.2^{+0.9}_{-0.9}$	S
RXJ085340.52+134924.9	rp700887n00	17.7	8.2	1.5	28.0	0.9	40	22	44	109	14.3	1.9	2.0	$-0.19^{+0.23}_{-0.34}$	1.00	$12.0^{+1.0}_{-1.2}$	S
RXJ085420.97+135439.6	rp700887n00	17.7	17.4	10.8	5.5	0.7	54	33	3	17	20.4	2.7	2.8	$-2.07^{+2.25}_{-2.77}$	0.86	$1.8^{+0.9}_{-0.6}$	S
RXJ085851.49+141150.7	rp700436n00	18.7	3.8	2.8	11.8	2.1	36	15	10	42	14.0	1.8	1.6	$-1.32^{+0.82}_{-0.84}$	1.00	$4.0^{+0.8}_{-0.6}$	S
RXJ085906.68+140307.2	rp700436n00	18.7	8.6	5.9	7.5	4.1	54	20	10	27	31.5	4.0	3.6	$-1.06^{+0.85}_{-1.29}$	0.99	$2.4^{+0.7}_{-0.5}$	I
RXJ085934.64+141457.6	rp700436n00	18.7	14.3	6.4	13.5	0.9	54	23	27	73	29.8	3.8	3.4	$-0.65^{+0.37}_{-0.57}$	1.00	$7.8^{+1.1}_{-0.8}$	I

Table 3. continued

1 Source	2 ROR	3 Exp (ks)	4 Offax (")	5 Perr (')	6 σ	7 PSF $\chi^2_{/\nu}$	8 r "	9 c1	10 c2	11 c3	12 b1	13 b2	14 b3	15 α	16 P < 0.5	17 Flux 0.5-2	18 Spl
RXJ090518.27+335006.0	rp700326n00	13.5	17.9	8.5	9.2	2.4	54	21	8	43	18.2	3.8	2.3	$-2.43^{+1.80}_{-1.09}$	1.00	$7.6^{+2.3}_{-1.3}$	S
RXJ090923.64+423629.2	rp700329a01	18.8	17.6	4.0	12.6	1.6	54	51	47	49	37.1	6.4	3.9	$0.23^{+0.20}_{-0.22}$	0.93	$7.4^{+1.0}_{-0.9}$	S
RXJ090926.82+541429.2	rp201382n00	31.5	9.5	5.0	10.7	5.7	25	12	16	28	12.5	1.7	1.2	$-0.13^{+0.43}_{-0.50}$	0.97	$2.2^{+0.4}_{-0.4}$	I
RXJ091006.80+425449.8	rp700329a01	18.8	6.1	4.7	9.6	1.0	36	23	14	25	22.6	3.9	2.4	$-0.40^{+0.61}_{-0.68}$	0.99	$2.4^{+0.6}_{-0.4}$	I
RXJ091049.66+430405.5	rp700329a01	18.8	17.2	5.3	9.3	1.7	54	45	32	44	44.7	7.8	4.7	$-0.20^{+0.34}_{-0.40}$	1.00	$5.7^{+0.9}_{-0.8}$	I
RXJ091908.27+745305.6	rp700882n00	10.8	13.6	9.1	8.6	1.2	50	18	11	28	14.0	2.4	2.2	$-0.35^{+0.54}_{-0.82}$	0.98	$4.7^{+1.0}_{-0.9}$	S
RXJ092103.75+621504.3	rp700211n00	16.0	3.8	4.1	10.2	1.7	32	9	14	28	8.6	1.8	1.3	$-0.02^{+0.50}_{-0.63}$	0.90	$3.4^{+0.6}_{-0.7}$	S
RXJ094144.51+385434.8	rp700387n00	15.8	7.7	6.5	8.5	1.3	54	35	17	19	38.7	4.7	3.8	$-0.12^{+0.57}_{-0.58}$	0.95	$2.1^{+0.5}_{-0.5}$	S
RXJ094356.53+164244.1	rp400141n00	8.2	12.0	6.2	7.4	0.6	54	13	7	19	11.0	2.1	1.9	$-0.44^{+0.80}_{-1.32}$	0.94	$4.1^{+1.2}_{-0.9}$	S
RXJ095029.49+733106.7	rp701214n00	8.4	17.0	12.2	6.0	0.9	54	11	7	20	9.7	1.8	1.7	$-0.65^{+0.70}_{-1.25}$	0.98	$5.3^{+1.4}_{-1.3}$	I
RXJ095340.67+074426.1	rp400059n00	6.5	13.7	11.3	6.0	1.4	54	5	9	14	9.0	1.5	1.3	$-0.38^{+0.52}_{-0.94}$	0.96	$4.3^{+1.2}_{-1.1}$	S
RXJ100923.93+543635.7	rp900213n00	12.4	11.4	4.5	12.7	1.5	54	64	21	44	38.2	7.9	4.0	$0.13^{+0.27}_{-0.25}$	0.97	$5.9^{+1.0}_{-0.9}$	S
RXJ100946.60+553658.3	rp900215n00	15.1	9.2	11.0	4.9	0.9	54	42	14	17	40.0	4.2	3.4	$-0.13^{+0.50}_{-0.68}$	0.96	$1.9^{+0.5}_{-0.5}$	I
RXJ101008.53+513334.9	rp700265a01	14.3	11.5	10.7	6.0	1.2	50	34	17	17	36.8	4.9	2.7	$-0.28^{+0.57}_{-0.56}$	0.99	$2.3^{+0.6}_{-0.6}$	S
RXJ101009.05+525901.5	rp700263n00	11.7	14.0	10.3	8.3	2.1	54	40	10	24	31.4	3.1	2.5	$-0.17^{+0.53}_{-0.81}$	0.98	$3.5^{+0.9}_{-0.7}$	S
RXJ101028.63+512841.2	rp700265a01	14.3	16.5	16.6	4.1	1.1	54	37	21	16	33.7	4.5	2.5	$0.10^{+0.36}_{-0.41}$	0.93	$3.0^{+0.7}_{-0.7}$	S
RXJ101031.05+503458.6	rp900214n00	12.4	10.5	21.5	4.7	0.8	54	41	13	21	33.4	4.6	3.1	$-0.06^{+0.44}_{-0.75}$	0.97	$2.8^{+0.8}_{-0.6}$	I
RXJ101033.47+533922.5	rp700264n00	13.5	6.1	8.5	6.0	1.1	36	15	9	14	13.2	1.3	0.9	$-0.24^{+0.56}_{-0.58}$	0.98	$2.0^{+0.5}_{-0.5}$	S
RXJ101058.91+534005.8	rp700264n00	13.5	7.9	7.3	6.4	1.7	32	13	9	17	12.2	1.2	0.9	$-0.45^{+0.57}_{-0.61}$	1.00	$2.5^{+0.6}_{-0.6}$	I
RXJ101112.05+554451.3	rp900215n00	15.1	7.4	3.5	17.3	1.3	54	49	31	57	40.6	4.3	3.4	$-0.43^{+0.29}_{-0.29}$	1.00	$7.0^{+0.9}_{-0.9}$	I
RXJ101123.17+524912.4	rp700263n00	11.7	11.2	5.3	6.7	1.7	54	26	8	23	32.2	3.2	2.6	$-1.41^{+0.93}_{-1.22}$	1.00	$3.3^{+1.0}_{-0.9}$	S
RXJ101147.48+505002.2	rp900214n00	12.4	15.9	60.0	8.0	1.4	54	41	16	27	32.1	4.5	3.0	$-0.09^{+0.44}_{-0.47}$	0.99	$4.6^{+1.0}_{-0.8}$	S
RXJ101159.42+281407.7	rp000049n00	25.3	13.7	9.1	8.8	1.3	54	54	22	42	58.2	7.7	5.3	$-0.38^{+0.45}_{-0.82}$	0.98	$3.0^{+0.6}_{-0.4}$	S
RXJ103133.93-142157.1	rp700461n00	13.1	7.3	5.7	8.6	1.7	29	2	5	24	6.1	1.3	1.4	$-1.41^{+1.10}_{-1.33}$	0.99	$3.7^{+1.0}_{-0.9}$	S
RXJ103230.88-141925.2	rp700461n00	13.1	9.0	6.4	8.8	0.9	40	9	9	26	12.5	2.6	2.8	$-0.62^{+0.74}_{-1.32}$	0.94	$3.6^{+0.8}_{-0.8}$	S
RXJ104648.27+541235.4	rp300158n00	10.9	7.1	6.7	7.6	1.1	36	12	3	23	11.6	1.4	1.3	$-2.61^{+1.36}_{-1.63}$	1.00	$3.9^{+1.2}_{-1.0}$	S
RXJ104723.37+540412.6	rp300158n00	10.9	14.4	13.4	4.9	1.9	54	19	8	11	23.4	2.7	2.6	$-0.56^{+0.90}_{-1.09}$	0.98	$1.7^{+0.7}_{-0.6}$	S
RXJ110210.03+251418.8	rp300291n00	41.8	11.8	5.5	8.8	0.7	54	113	28	52	105.1	10.8	6.1	$-0.33^{+0.53}_{-0.58}$	0.99	$2.1^{+0.3}_{-0.3}$	S
RXJ110228.24+250327.1	rp300291n00	41.8	3.1	1.1	26.4	1.4	29	38	45	127	31.2	3.2	1.8	$-0.71^{+0.31}_{-0.25}$	1.00	$5.8^{+0.5}_{-0.5}$	S
RXJ110231.12+355342.7	rp200127a01	10.1	13.8	19.4	4.0	0.6	54	19	10	14	24.6	3.1	2.5	$-0.34^{+0.69}_{-0.99}$	0.95	$2.5^{+0.8}_{-0.8}$	I
RXJ110244.57+250959.4	rp300291n00	41.8	5.3	9.6	4.4	0.8	43	62	17	20	74.5	7.7	4.4	$-0.47^{+0.96}_{-0.84}$	0.98	$0.8^{+0.2}_{-0.2}$	I
RXJ110431.75+355208.5	rp200127a01	10.1	17.1	12.2	5.1	1.0	54	23	10	16	24.3	3.0	2.4	$-0.21^{+0.63}_{-1.02}$	0.94	$3.5^{+1.1}_{-0.9}$	S
RXJ110452.52+360414.8	rp200127a01	10.1	18.0	11.4	7.3	0.9	54	24	13	23	24.4	3.0	2.5	$-0.26^{+0.67}_{-0.63}$	0.97	$5.5^{+1.3}_{-1.1}$	S
RXJ110707.63+723634.8	rp700872n00	10.0	2.8	9.2	4.5	1.2	29	3	4	9	6.6	1.0	1.3	$-0.59^{+0.96}_{-1.44}$	0.93	$1.5^{+0.7}_{-0.5}$	S
RXJ110742.05+723236.0	rp700872n00	10.0	4.4	2.7	16.1	0.5	47	24	20	45	15.8	2.3	3.2	$0.12^{+0.37}_{-0.45}$	0.90	$8.1^{+1.2}_{-1.1}$	S
RXJ111750.51+075712.8	rp700358n00	13.6	12.8	2.1	24.4	2.4	47	20	51	103	17.9	2.8	2.1	$-0.15^{+0.23}_{-0.29}$	1.00	$16.5^{+1.6}_{-1.4}$	S
RXJ111926.34+210646.1	rp700228n00	20.1	13.0	3.5	12.6	1.5	54	76	47	58	48.9	8.3	4.6	$0.29^{+0.18}_{-0.19}$	0.90	$5.9^{+0.7}_{-0.7}$	S
RXJ111935.63+133407.4	rp700010n00	13.2	10.1	5.9	6.2	1.2	54	22	14	21	34.9	5.5	3.2	$-0.72^{+0.67}_{-1.03}$	0.99	$2.7^{+0.7}_{-0.7}$	S
RXJ111942.16+211518.1	rp700228n00	20.1	8.5	4.3	12.0	2.3	54	61	35	37	52.5	8.9	4.9	$0.13^{+0.30}_{-0.30}$	0.95	$3.4^{+0.6}_{-0.5}$	S
RXJ112056.87+132726.2	rp700010n00	13.2	12.6	12.2	4.9	0.8	54	27	6	15	33.1	5.2	3.0	$-1.65^{+1.48}_{-2.12}$	0.99	$1.7^{+0.8}_{-0.6}$	S
RXJ112838.96-041628.0	rp700372n00	15.7	12.1	7.4	4.6	3.1	54	19	9	17	30.9	4.2	2.7	$-0.63^{+1.01}_{-1.47}$	0.94	$1.9^{+0.6}_{-0.5}$	S
RXJ113624.52+295952.8	rp200091n00	25.1	12.0	5.9	7.2	1.6	47	35	12	33	35.9	6.2	3.3	$-1.28^{+1.03}_{-1.32}$	1.00	$2.3^{+0.6}_{-0.5}$	I
RXJ114621.27+285320.6	rp300287n00	15.9	11.0	19.1	4.6	1.5	43	21	15	16	23.1	2.5	2.0	$0.05^{+0.44}_{-0.56}$	0.90	$2.2^{+0.5}_{-0.5}$	S
RXJ114654.52+283939.9	rp300287n00	15.9	4.8	6.2	10.3	3.1	54	49	14	35	39.1	4.3	3.4	$-0.19^{+0.69}_{-0.73}$	0.97	$3.6^{+0.8}_{-0.6}$	I
RXJ114708.66+283001.2	rp300287n00	15.9	14.9	12.7	6.9	1.6	47	21	12	22	25.0	2.7	2.2	$-0.47^{+0.74}_{-0.63}$	0.99	$3.0^{+0.7}_{-0.6}$	S
RXJ114736.94+284131.4	rp300287n00	15.9	10.6	4.9	8.1	0.9	54	37	13	22	38.0	4.2	3.3	$-0.30^{+0.63}_{-0.85}$	0.97	$2.4^{+0.7}_{-0.5}$	S
RXJ115952.10+553212.1	rp700055n00	44.7	17.2	1.4	73.6	6.1	54	418	410	698	107.0	15.9	9.7	$0.17^{+0.05}_{-0.04}$	1.00	$40.1^{+1.5}_{-1.2}$	S
RXJ120403.79+280711.2	rp700232n00	12.5	15.8	1.1	38.1	12.6	54	156	123	246	36.4	11.1	4.5	$0.38^{+0.09}_{-0.07}$	0.95	$44.9^{+2.9}_{-2.2}$	S
RXJ120515.93-033424.6	rp201367m01	45.3	13.8	6.7	12.9	1.7	54	98	33	79	91.2	11.9	6.7	$-0.64^{+0.53}_{-0.61}$	1.00	$3.2^{+0.4}_{-0.4}$	I
RXJ121017.25+391822.6	rp700277n00	19.0	6.8	5.9	8.9	1.7	54	82	37	52	77.2	13.3	7.0	$-0.02^{+0.35}_{-0.49}$	0.97	$4.6^{+0.7}_{-0.7}$	S
RXJ121115.30+391146.8	rp700277n00	19.0	15.4	4.4	20.9	1.7	40	52	81	87	36.7	6.3	3.3	$0.27^{+0.15}_{-0.17}$	0.95	$15.7^{+1.3}_{-1.5}$	S
RXJ121803.82+470854.6	rp600546n00	19.9	13.3	12.4	4.3	2.2	54	45	12	18	53.3	4.3	3.8	$-0.52^{+0.60}_{-1.07}$	0.99	$1.5^{+0.4}_{-0.4}$	S
RXJ121834.72+300957.2	rp700221n00	18.6	10.0	5.1	7.7	0.9	32	13	15	18	17.7	3.3	2.3	$-0.19^{+0.45}_{-0.68}$	0.96	$2.1^{+0.5}_{-0.5}$	S
RXJ124913.86-055906.2	rp600262a02	35.2	14.6	9.0	6.9	0.6	43	51	30	41	51.0	12.4	7.1	$-0.09^{+0.57}_{-0.55}$	0.96	$2.4^{+0.5}_{-0.4}$	S
RXJ124919.66-060430.2	rp700375n00	10.1	5.3	5.2	7.6	0.9	50	24	21	23	27.7	7.4	3.6	$-0.20^{+0.63}_{-0.60}$	0.97	$4.0^{+1.0}_{-0.8}$	S
RXJ124949.92+405305.2	rp600050n00	73.0	17.7	7.6	8.8	1.7	54	361	198	124	341.6	133.1	25.0	$0.08^{+0.26}_{-0.35}$	0.98	$3.5^{+0.4}_{-0.4}$	S

Table 3. continued

1 Source	2 ROR	3 Exp (ks)	4 Offax (")	5 Perr (')	6 σ	7 PSF $\chi^2_{/\nu}$	8 r "	9 c1	10 c2	11 c3	12 b1	13 b2	14 b3	15 α	16 P < 0.5	17 Flux 0.5-2	18 Spl
RXJ125447.96+563842.3	rp700208n00	18.2	17.9	16.6	5.1	0.6	54	68	25	42	60.3	11.4	5.9	$-0.23^{+0.41}_{-0.76}$	0.99	$5.0^{+1.0}_{-0.8}$	I
RXJ125556.56+565850.9	rp700208n00	18.2	7.1	8.8	4.8	0.7	54	58	23	22	73.2	13.8	7.2	$-0.69^{+0.93}_{-1.31}$	0.99	$1.6^{+0.6}_{-0.5}$	S
RXJ131047.80+322958.1	rp700216a00	7.7	9.8	3.4	12.0	1.0	54	25	16	28	21.4	3.2	2.2	$-0.32^{+0.50}_{-0.44}$	1.00	$6.5^{+1.3}_{-1.2}$	S
RXJ131635.62+285942.7	rp100308n00	19.9	6.8	1.8	28.2	10.7	54	158	92	143	54.7	7.2	3.9	$0.35^{+0.10}_{-0.08}$	0.96	$13.7^{+1.0}_{-1.0}$	S
RXJ131646.89+285721.1	rp100308n00	19.9	10.0	4.6	11.8	3.9	54	71	26	38	55.6	7.3	4.0	$0.11^{+0.28}_{-0.38}$	0.96	$3.3^{+0.6}_{-0.5}$	S
RXJ131651.64+291251.1	rp100308n00	19.9	9.1	3.0	13.0	1.2	54	72	21	37	54.2	7.1	3.9	$0.13^{+0.30}_{-0.45}$	0.94	$3.0^{+0.5}_{-0.5}$	I
RXJ131653.87+291708.8	rp100308n00	19.9	12.9	6.7	8.3	1.0	54	52	15	16	56.4	7.4	4.0	$-0.31^{+0.67}_{-1.29}$	0.96	$1.2^{+0.4}_{-0.4}$	I
RXJ131721.79+291119.1	rp100308n00	19.9	13.7	14.3	6.8	1.4	54	56	18	28	55.5	7.3	4.0	$-0.40^{+0.48}_{-0.88}$	0.99	$2.4^{+0.6}_{-0.5}$	I
RXJ133146.37+111420.4	rp701034n00	9.4	12.0	14.5	5.0	0.6	50	21	8	23	21.5	4.9	3.5	$-1.47^{+1.30}_{-1.61}$	1.00	$4.0^{+1.2}_{-1.2}$	S
RXJ133147.00+105653.0	rp701034n00	9.4	13.3	13.0	5.5	1.4	54	21	18	16	23.6	5.4	3.8	$0.07^{+0.42}_{-0.75}$	0.88	$3.2^{+0.9}_{-0.9}$	S
RXJ133152.51+111643.5	rp701034n00	9.4	12.7	1.0	36.5	1.0	54	27	57	273	23.7	5.4	3.8	$-1.71^{+0.27}_{-0.33}$	1.00	$57.0^{+4.1}_{-3.9}$	S
RXJ133948.81+482111.5	rp700473n00	9.5	15.9	12.9	7.1	0.9	54	19	12	23	20.0	2.7	2.1	$-0.48^{+0.68}_{-0.65}$	0.99	$5.3^{+1.2}_{-1.2}$	I
RXJ134335.29-001643.7	rp701000a01	24.7	2.6	4.0	7.2	0.6	54	45	21	19	57.9	9.5	6.0	$-0.19^{+0.57}_{-1.07}$	0.94	$1.1^{+0.4}_{-0.3}$	I
RXJ134905.63+600037.4	rp600270n00	35.7	10.8	5.8	6.2	1.6	54	84	14	26	82.7	7.6	4.4	$-0.61^{+0.94}_{-1.37}$	0.97	$1.2^{+0.3}_{-0.3}$	I
RXJ135105.69+601538.5	rp600270n00	35.7	14.5	5.6	12.4	2.2	54	78	44	65	80.0	7.4	4.3	$-0.12^{+0.33}_{-0.27}$	1.00	$3.8^{+0.4}_{-0.4}$	S
RXJ135529.59+182413.6	rp700392n00	11.0	8.0	6.2	8.5	0.6	54	28	16	25	27.8	7.5	4.2	$-0.41^{+0.84}_{-0.94}$	0.98	$3.6^{+0.9}_{-0.9}$	S
RXJ140134.94+542029.2	rp600108n00	21.3	13.8	9.8	6.5	1.6	54	89	34	39	87.5	15.8	9.1	$-0.13^{+0.46}_{-0.59}$	0.98	$2.9^{+0.6}_{-0.6}$	S
RXJ140416.61+541618.2	rp600108n00	21.3	10.6	4.3	8.7	1.3	54	90	40	37	92.7	16.8	9.7	$-0.07^{+0.34}_{-0.56}$	0.98	$2.8^{+0.6}_{-0.5}$	S
RXJ142754.71+330007.0	rp200329n00	23.9	14.7	18.1	7.6	2.0	54	83	26	38	65.9	7.7	4.2	$0.21^{+0.27}_{-0.39}$	0.90	$3.0^{+0.5}_{-0.5}$	S
RXJ150132.45-082507.2	rp200510n00	11.3	10.5	2.2	17.0	1.2	54	23	27	92	23.2	14.4	6.5	$-1.78^{+0.87}_{-0.94}$	1.00	$15.7^{+2.6}_{-2.0}$	S
RXJ163054.25+781105.1	rp170154n00	26.0	7.5	1.5	25.5	2.0	25	21	40	106	12.5	2.6	1.2	$-0.01^{+0.37}_{-0.29}$	0.98	$9.0^{+0.7}_{-0.9}$	S
RXJ163308.57+570258.7	rp200721n00	37.8	11.9	7.3	8.8	1.6	54	131	30	42	134.6	11.9	7.3	$-0.11^{+0.42}_{-0.69}$	0.95	$1.9^{+0.3}_{-0.3}$	S
RXJ170041.60+641259.0	rp701457n00	20.5	2.2	2.2	36.4	23.6	47	95	145	282	32.7	3.3	3.2	$0.17^{+0.11}_{-0.10}$	1.00	$27.0^{+1.3}_{-1.5}$	S
RXJ170044.36+520545.6	rp700123n00	6.6	17.7	8.9	6.4	1.2	54	13	8	17	11.8	2.0	1.3	$-0.20^{+0.61}_{-1.13}$	0.93	$6.1^{+1.8}_{-1.3}$	S
RXJ170123.32+641413.0	rp701457n00	20.5	3.4	2.0	27.0	18.4	43	69	93	172	27.9	2.8	2.7	$0.24^{+0.13}_{-0.13}$	0.99	$16.6^{+1.2}_{-1.0}$	S
RXJ171112.30+710924.7	rp700875n00	24.1	12.2	11.7	4.9	1.1	50	33	14	28	36.5	6.9	3.7	$-0.62^{+0.80}_{-1.41}$	0.95	$2.1^{+0.6}_{-0.4}$	S
RXJ204640.48-363147.5	rp201374a01	25.3	13.6	4.1	15.6	2.3	54	57	48	82	63.8	13.4	7.2	$-0.14^{+0.45}_{-0.36}$	0.98	$6.3^{+0.7}_{-0.7}$	S
RXJ204716.74-364715.1	rp201374a01	25.3	13.2	3.8	19.7	2.3	54	69	48	123	64.1	13.5	7.3	$-0.64^{+0.35}_{-0.53}$	1.00	$9.1^{+0.9}_{-0.9}$	S
RXJ213807.61-423614.3	rp701180a01	2.2	14.1	7.2	8.3	0.5	54	5	6	19	5.8	1.3	0.7	$-1.10^{+0.92}_{-1.06}$	1.00	$16.7^{+5.1}_{-3.6}$	S
RXJ223619.89-261426.2	rp700873n00	22.9	13.8	11.9	4.7	1.0	54	62	19	28	72.0	8.4	5.3	$-0.61^{+0.61}_{-0.96}$	0.99	$2.1^{+0.4}_{-0.6}$	S
RXJ223654.00-261230.6	rp700873n00	22.9	18.1	11.2	5.1	0.6	54	45	17	41	56.3	6.6	4.2	$-1.24^{+0.74}_{-0.80}$	1.00	$4.1^{+0.9}_{-0.7}$	S
RXJ225018.97+242750.8	rp201552n00	15.8	9.2	4.1	8.2	2.1	54	3	12	26	11.2	2.9	2.8	$-0.59^{+0.62}_{-0.91}$	0.98	$2.9^{+0.7}_{-0.5}$	S
RXJ230248.28+084348.1	rp700423n00	16.6	10.6	2.8	10.9	1.9	50	19	33	58	22.1	3.8	4.8	$0.13^{+0.32}_{-0.46}$	0.88	$7.0^{+1.0}_{-0.8}$	I
RXJ232505.73+234056.5	rp200322n00	22.6	17.3	12.5	5.7	1.2	54	26	16	40	26.5	8.8	8.0	$-0.88^{+0.99}_{-1.36}$	0.97	$3.6^{+0.8}_{-0.8}$	I
RXJ235113.89+201347.3	rp701217a01	5.6	7.4	2.2	28.1	1.8	54	9	31	91	5.5	1.5	1.5	$-0.55^{+0.29}_{-0.44}$	1.00	$30.3^{+3.2}_{-3.1}$	S

Description of columns in Table 3 (see Sec 2)

1) Source name based on J2000 coordinates of *ROSAT* source from PSS
2) *ROSAT* observation in which source was detected
3) *ROSAT* PSPC exposure time in kiloseconds after good time screening
4) Offaxis angle of source in arcminutes
5) Positional uncertainty of source in arcseconds from PSS
6) PSS significance of source above background level in units of σ
7) $\chi^2_{/\nu}$ from a fit of the model PSPC point spread function to the source radial profile in 5 arcsecond bins out to 1 arcminute
8) Source circle radius in arcseconds for extraction of 3 colour spectrum
9) Number of counts in PSPC channels 11-41 within the source circle
10) Number of counts in PSPC channels 52-90 within the source circle
11) Number of counts in PSPC channels 91-201 within the source circle
12) Expected number of background counts in PSPC channels 11-41 within the source circle
13) Expected number of background counts in PSPC channels 52-90 within the source circle
14) Expected number of background counts in PSPC channels 91-201 within the source circle
15) Fitted power law spectral slope with 68% uncertainty
16) Probability of source having spectral slope $\alpha <$ (harder than) 0.5
17) 0.5 - 2 keV flux and 68% uncertainty in units of 10^{-14} erg cm^{-2} s^{-1}
18) Optical counterpart flag: 'S' means spectroscopic sample, 'I' means imaging sample